Sensors & Diagnostics

PAPER

View Article Online
View Journal | View Issue

Cite this: *Sens. Diagn.*, 2026, **5**, 248

Reproducible single-molecule optofluidic-SERS analysis on nanostar-activated diatom biosilica capsules

Subhavna Juneja, Sudipta Biswas, Kang Rong and Alan X. Wang *

Single-molecule (SM) analysis with surface-enhanced Raman scattering (SERS) usually requires sophisticated engineering on plasmonic nanostructures to provide extremely strong hot-spots to enhance the intrinsically weak signal. In this work, we report a cell-sized biosilica capsule based on the diatom *Pinnularia* sp. frustule decorated with high-density bimetallic nanostars consisting of gold and silver, capable of achieving reproducible single-molecule SERS analysis. Such a plasmonic nanostar-activated biological photonic crystal nanostructure synthesized by a simple self-assembly method enhances hot-spots universally, which is proved by finite difference time domain simulation. The cell-sized biosilica capsule also concentrates trace-levels of target molecules from ultra-small fluidic droplets through a drop-on-demand inkjet-printing technique. We experimentally demonstrated reproducible SM optofluidic-SERS sensing from 120 nL of 10^{-15} M rhodamine 6G solution containing only 72 molecules through statistical analysis of mapping data over the cell-sized biosilica capsule, achieving a 3× higher signal-to-noise ratio and 9× better SM detection possibility compared to that on the glass substrate.

Received 3rd September 2025,
Accepted 25th November 2025

DOI: 10.1039/d5sd00161g

rsc.li/sensors

Introduction

Single-molecular detection holds scientific and practical interests across various fields.[1–3] Surface enhanced Raman spectroscopy (SERS), given its molecular specificity and plasmonic enhancement has been sought as a robust spectroscopic technique for achieving ultra-sensitive analyte tracing, scaling to single-molecule (SM) sensing.[4] However, SM SERS analysis requires extremely engineered plasmonic nanostructures such as crevices,[5] interparticle junctions[6] or sharp pointed edges[7] known as 'hot spots', where light concentration is high, resulting in dramatic electric-field enhancement factors (EFs) and thus, Raman signal enhancement.[8] Plasmonic nanoparticles assembled as dimer or multimer structures, at the nanoscale junctions, have been established to achieve local EF enhancement ranging 10^8–10^{10}, enabling SM detection.[9] However, tailoring a strategic design and engineering precisely controlled nanoscale gap junctions often requires complex fabrication, limiting its real-world applicability.

Anisotropic nanostructures, unlike spherical nanoparticles, are inherently rich in hot spots owing to their irregular shapes and high aspect ratios.[10] Amongst different anisotropic features, such as nanotubes,[11] nanoprisms,[12] and urchin-shaped structures,[13] a star-like morphology[14–16] comprising sharp tips protruding from a spherical central core has emerged as an excellent SERS substrate. At the acute tip termini, facilitated *via* the lightning rod effect[17] (more charge accumulation), stronger localised plasmon resonance can be established producing excellent opportunity for hot spot creation. A single star-shaped nanostructure with multiple tip ends can thus have multiple hot spots within the same structure circumventing the need for nanogap engineering for hot spot creation. Plasmonic nanostars, predominantly gold, have seen great success as SERS substrates, where detection levels as low as femtomolar have been achieved.[18–22] Although highly sensitive, their affinity for aggregation and lack of reliable signal generation originating from inhomogeneous substrates have restricted their practical use. In addition to hot-spot engineering, plasmonic nanostructures are often integrated with porous micro- or nano-scale dielectric structures that act as scaffolds addressing aggregation by limiting interparticle proximity while being anchored to the porous surface and improving analyte adsorption due to their high surface area and thus, SERS efficiency.[23,24]

Diatoms, marine photosynthetic algae, present an exemplary case of such scaffolds in their porous silica shell.[25] The intricately patterned cell walls, also known as "frustules", consist of a hierarchical arrangement of porous structures resembling a high-density array of mesopores like in a capsule.[26] These nature-created biosilica capsules have been previously known to not only provide the surface for uniform

Department of Electrical and Computer Engineering, Baylor University, Waco, TX 76706, USA. E-mail: alan_wang@baylor.edu

nanostructure anchoring but also contribute to augmented SERS signals by a) intensifying localised surface plasmon resonance (LSPR) through guided-mode resonances at visible wavelengths and b) higher adsorption capacity driven by their porosity, high surface area and hydrophilic nature.[26,27] In a series of experimental and simulation studies conducted by our research group previously, these biosilica capsules conjugated with plasmonic nanoparticles like silver (Ag) and gold (Au) have been shown to achieve SERS sensitivity improvement by orders of magnitude.[28] However, despite achieving ultra-sensitive screening for various analytes,[29,30] they still fall short of achieving SM sensitivity at a universal level. To address this, we designed a hybrid SERS substrate by conjugating diatom *Pinnularia* sp. biosilica capsules with bimetallic star-like nanostructures to achieve superior SERS efficiency – both in sensitivity and reproducibility. Bimetallic nanostars, of Au for anisotropy and Ag for higher plasmon scattering, synthesised using a chemical route[31] were self-assembled onto the biosilica capsules using (3-aminopropyl)-triethoxysilane (APTES) to obtain hybrid SERS substrates. Through a series of simulation tests conducted, the hybrid SERS substrates show a significantly higher local EF resulting in better SERS performance. The improved EF was accredited to the collective contribution of the intrinsic hot-spot richness in the nanostars and an overall global increase in hot-spot regions on the biosilica capsules due to nanostars anchored onto the structure.

Another bottleneck to achieve SM detection is the slow diffusion rate of analytes due to inadequate mass transfer at such low concentrations,[26] which often makes it difficult to obtain statistically significant signals. To accelerate mass transfer, we used a drop-on-demand inkjet printing device to deliver analytes for ultra-efficient optofluidic-SERS sensing. Printing successive small analyte droplets allows us to locally accumulate the analyte on the biosilica capsule ensuring enough analyte molecules in the detection volume for reproducible and reliable signals. Each capsule, averaged 20 × 6 μm^2 in size with self-assembled bimetallic nanostars, serves as a highly sensitive SERS substrate individually. The achieved local enrichment is postulated to be a cumulative outcome of the hydrophilic nature of the biosilica capsule, shrinking of the depinning contact line limiting the physical boundaries of analyte distribution and a thermal Marangoni recirculation effect as noted in our previous report.[32] At an LOD concentration of 10^{-15} M, a total of only 120 nL of the R6G solution containing only 72 molecules was used to acquire SERS signals as our optofluidic-SERS model analyte. Considering the 100 μm diameter of the inkjet dispenser and the 1.03 μm diameter laser spot of our confocal Raman microscope, the probability of detecting a single R6G molecule is 1/130. We conducted multiple 10 × 10 SERS mapping measurements over biosilica capsules, and statistical analysis confirmed a 3× higher signal-to-noise ratio and 9× better SM detection possibility compared to nanostars on a glass substrate. By allowing consistent data recording, specifically at very low analyte mass values, discrepancy in data generation (hot spot ambiguity in concentration-based methods) and statistical unreliability (dilution errors, molecule diffusion, surface adsorption, *etc.*) can be largely addressed, opening avenues for real world applicability of the SERS sensing platforms. In addition to the excellent SERS performance, the present work also finds significance in exploring a relatively less studied nanocomposite system in the fabricated biosilica–nanostar complex. They not only carry a low carbon footprint but are also cost-effective and possess light modulating characteristics as noted, both from our experimental and numerical studies. Although at infancy, the presented bimetallic nanostar–biosilica capsules hold great potential as light-modulating modules with wide applicability. We thus foresee this study to guide not only improved SERS sensing platforms but also designing of newer engineered nanomaterials.

Materials and methods

Materials and chemicals

Chloroauric acid ($HAuCl_4$), silver nitrate ($AgNO_3$, 99.8%), L-ascorbic acid, hydrochloric acid (HCl), R6G, NaCl, Na_2SO_4, KCl, $NaHCO_3$, NaBr, H_3BO_3, NaF, $MgCl_2{\cdot}6H_2O$, $CaCl_2{\cdot}2H_2O$, $SrCl_2{\cdot}6H_2O$, $Na_2MoO_4{\cdot}2H_2O$, $ZnSO_4{\cdot}7H_2O$, $CuSO_4{\cdot}5H_2O$, $CoCl_2{\cdot}6H_2O$, $MnCl_2{\cdot}4H_2O$, $FeCl_3{\cdot}6H_2O$, ethylenedinitrol tetraacetic acid disodium salt ($C_{10}H_{14}O_8N_2Na_2{\cdot}2H_2O$), cyanocobalamin, biotin, thiamine HCl, $NaNO_3$, $NaH_2PO_4{\cdot}H_2O$, and $Na_2SiO_3{\cdot}9H_2O$ were purchased from Sigma-Aldrich. All reagents were of analytical grade and used as received without further treatment. Milli-Q deionized water (18.2 MΩ) was used to prepare all the solutions unless mentioned otherwise.

Analyte printing

An inkjet printing system was utilized to print the analyte onto our biosilica capsule SERS substrates. Key device components comprising the printing head, fluid channels, printing controller and software were purchased from MicroFab Technologies Inc. (TX, USA). The printing processes were controlled *via* the Jet Server4 program version 4.1. For all dispensing experiments, glass tubing with a tip orifice diameter of 50 μm was used. For each experiment, depending on the analyte concentration, the number of droplets varying between 1 and 2000 were dispensed onto the biosilica capsule. Each droplet was maintained at a volume of 60 picolitres (pL) while the injection interval between consecutive droplets was 3 seconds. A dwell time of 25 μs with an echo time of 50 μs helped to achieve a near spherical droplet morphology. Whereas, maintaining a dwell and echo voltage of 25 V and −25 V, respectively, ensured the appropriate droplet speed.

Raman measurements

For each R6G dye concentration, ranging from 10^{-6} M to 10^{-15} M, different number of droplets were printed onto the biosilica capsule. The detailed description of the droplet number and

Table 1 Estimation of R6G molecules tested during optofluidic SERS measurements at varying concentrations from 10^{-6} M to 10^{-15} M

R6G concentration	No. of droplets	Total volume	No. of molecules in the total volume of liquid dispensed	No. of molecules within the laser spot by assuming uniform analyte distribution
10^{-6} M	1	60 pL	36×10^6	36×10^4
10^{-8} M	10	600 pL	3.6×10^6	3.6×10^4
10^{-9} M	50	3 nL	1.7×10^6	1.7×10^4
10^{-10} M	500	30 nL	1.7×10^6	1.7×10^4
10^{-12} M	1000	60 nL	3.6×10^4	3.6×10^2
10^{-15} M	2000	120 nL	72	1/130

Abbreviations: pL – pico-litre; nL – nano-litre.

the corresponding effective R6G concentration is provided in Table 1. After the requisite volume was printed, the SERS substrates were measured using a Horiba XploRA Plus Confocal Raman system equipped with a CCD detector and a 50× objective lens. The laser excitation used was 638 nm with an estimated laser spot diameter of 1.03 μm. The acquisition time and laser power for each measurement both spectral and mapping were kept consistent at 0.5 seconds and 1%, respectively. SERS mapping images were acquired with a 10 × 10 point mapping. The spectra were collected over a range from 400 to 2000 cm^{-1}. For SERS spectral data, each spectrum for every concentration is an average of 10 recorded spectra. For mapping data, for each R6G concentration, except for 10^{-15} M, 5 different diatoms were chosen for statistical significance and reproducibility. For the lowest R6G concentration tested *i.e.* 10^{-15} M, a total of 10 different diatoms were mapped to acquire the data. All SERS spectra were recorded using LabSpec6 software and processed on Origin for final image presentation.

Results and discussion

Characterization of the SERS nanomaterial

Morphological details and adhesion of the nanostructures onto the biosilica capsule was investigated using electron

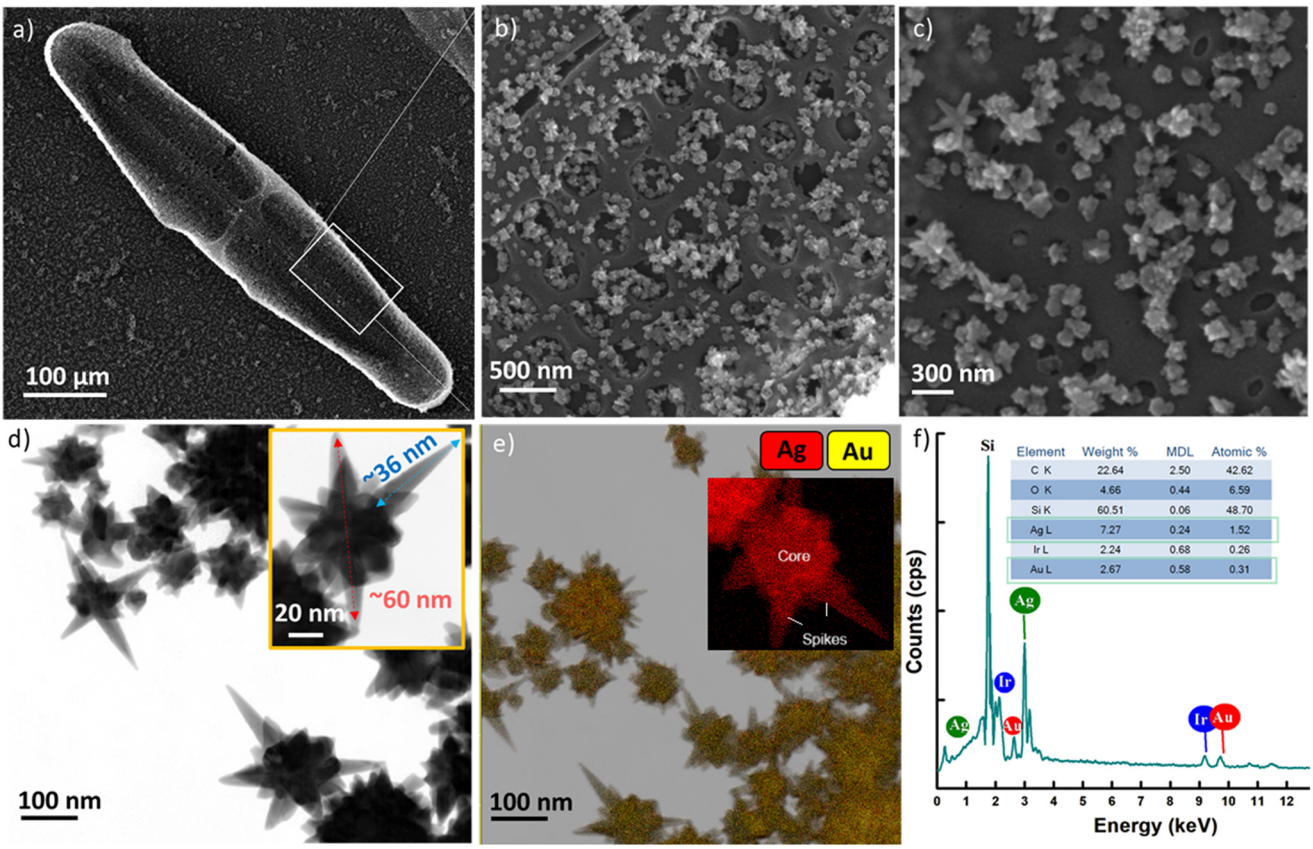

Fig. 1 a) Representative SEM image of a diatom *Pinnularia* sp. frustule with self-assembled bimetallic nanostars showing an overview of the capsule; (b and c) higher magnification SEM images of the hybrid plasmonic–biosilica capsule with uniformly distributed bimetallic nanostars on the surface and inside the nanopores of the frustule. Representative TEM images d) EDS elemental mapping with zoomed-in view of nanstars in the inset figure, e) EDS image with zoomed-in view of the nanostar in the inset figure, and f) the EDS dispersive spectra of the bimetallic nanostars.

microscopy. The scanning electron microscopy (SEM) images (Fig. 1a–c) acquired at different magnifications show a representative hybrid capsule consisting of the diatom *Pinnularia* sp. frustule with self-assembled bimetallic star-like nanostructures, indicating successful adhesion. The magnified SEM images in Fig. 1b and c reveal that bimetallic nanostars are uniformly distributed not only on the surface but also inside the nanopores of the biosilica capsule, generating ample hot spots to improve the overall electric field enhancement. Importantly, in transferring the colloidal stars onto the solid capsule, the overall star-like morphology of the nanostructures with a central core and protruding spiked ends was retained. In view of the technical limitations of SEM in observing the morphology of the nanostructures clearly, transmission electron microscopy (TEM) was performed to gain further insights into the dimensions and elemental composition of the synthesized nanostars. Fig. 1d displays the TEM image of the bimetallic nanostars, where the overall dimension of the synthesized bimetallic nanostars, tip-to-tip was averaged to be 60 ± 10 nm. The spike length, measured from the surface of the core to the tip of the nanostar was determined to be 33 ± 5 nm while the branch tip diameter was measured to be 7 ± 0.9 nm (inset of Fig. 1d). To analyse the elemental and spatial distribution of Au and Ag, elemental mapping and energy dispersive X-ray spectroscopy (EDS) were performed. Fig. 1e presents the EDS mapping where colours red and yellow represent Ag and Au, respectively, marking the presence of both metals in the synthesized nanostructures.

Ag was found to be evenly distributed throughout the nanostar surface with marginally thicker deposition (higher brightness) at the centre (inset of Fig. 1e). Ag by preferential binding and limiting the deposition of gold at the growth ends is known to tune the sharp edges, playing a role in stabilizing the morphology,[33] explaining its presence throughout the nanostar. While in the plating stage where excess Ag ions are present, Ag prefers to accumulate around the nanostructures' central region as this is energetically more favourable, resulting in a thicker core.[34] The EDS spectrum presented in Fig. 1f affirms the presence of Au and Ag. Compared to Au, the atomic percentage of Ag was observed to be ~5 times higher corroborating our observations made from the mapping micrographs. The additional peaks recorded in the spectrum were mapped to be originating from the coating (Ir) and solid substrates (C, O and Si) used for preparing the SERS substrates. No additional spectral peaks were recorded, confirming sample purity.

SERS EFs of the biosilica capsule are dependent on various factors (*nanoparticle size*, *morphology*, *and substrate roughness*) including their plasmon resonance peak maxima making it imperative to study their absorption character. Fig. 2a compares the LSPR between bare biosilica capsules (control), synthesized bimetallic nanostars as colloidal solution, and bimetallic nanostars self-assembled onto the capsules. The absorption spectrum of biosilica capsule–bimetallic nanostars shows a broad peak centred at a wavelength of 688 nm, which is significantly blue-shifted compared to the bimetallic nanostars in the colloidal state. This blue shift in the absorbance spectrum can be attributed to structural confinement that alters the surface plasmon characteristics of the anisotropic nanostars as they anchor themselves onto the biosilica capsule. Based on the hydrodynamic plasmon-polariton theory, nanostructures in the bound state, experience a strong plasmonic wave interaction from the surface electrons in their vicinity. This electronic interplay, strongly binding the nanostars to the adjoining surface, biosilica or SiO_2 in our case, establishes a requirement of higher energy (shorter wavelength) to bring them into a state of excitement, often resulting in a significant blue shift.[35] The bare diatom photonic crystals on the other hand were noted to show absorbance in the low UV-visible region with a broad absorption edge below 400 nm, a typical feature of the biosilica material.

Inferring from our UV-vis-NIR study, we postulated a 638 nm laser (closest excitation to the SERS material plasmon maxima) to be an ideal excitation source for achieving maximum SERS enhancement. Using a drop-on-demand inkjet printing device, 1 drop (~60 pL) of 10^{-6} M R6G dye

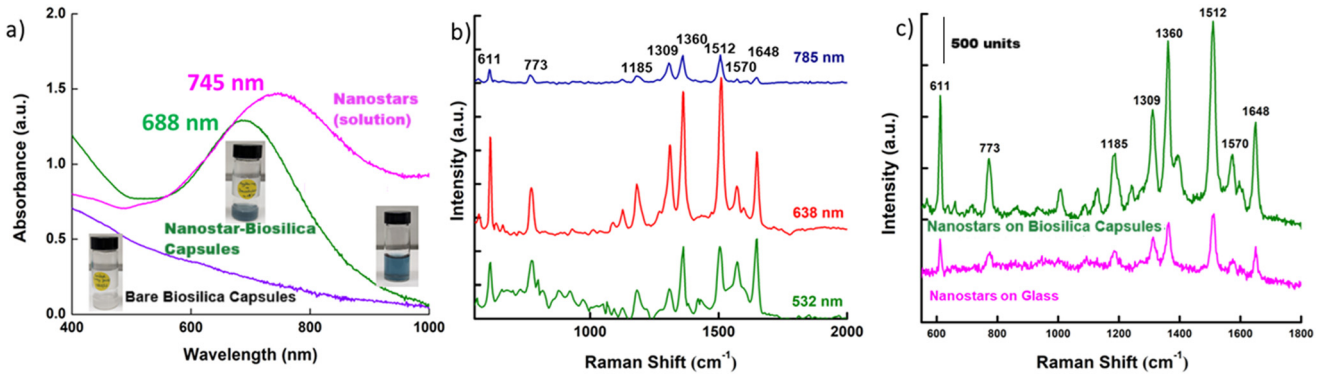

Fig. 2 a) UV-vis-NIR spectra and the corresponding photo images of the biosilica capsule, as-synthesized bimetallic nanostars in solution, and self-assembled nanostars on diatom frustules; b) representative SERS spectra of 1 drop of 10^{-6} M R6G printed on the capsule tested with different excitation wavelengths; and c) SERS spectra of 1 drop of 10^{-6} M R6G printed on bimetallic nanostars on glass (pink) and on a single capsule (green).

was printed onto a single plasmonic–biosilica capsule to record the spectra using three different lasers – 532 nm, 638 nm and 785 nm. As presented in Fig. 2b, for all the three tested wavelengths, characteristic R6G Raman vibrations of 611, 773, 1185, 1309, 1369, 1512, 1570, and 1648 cm^{-1} were noted. However, the signal strength was markedly different. The maximum SERS intensity was recorded with 638 nm due to its proximity to the absorption maximum of 688 nm for the hybrid SERS material, followed by 532 nm and 785 nm, respectively. As 532 nm is still higher energy compared to 688 nm, it could generate sufficient EFs. However, for 785 nm, the energy was too weak to bring any dramatic SERS enhancement. 638 nm excitation was thus selected as the optimal working wavelength for the subsequent experimental work.

Bimetallic nanostars are considered a superior SERS platform owing to their richness in hot spots. To verify the positive contribution from the photonic crystal properties of the biosilica capsules, a comparative SERS spectrum of R6G on bimetallic nanostars in the presence and absence of the capsule was recorded. Fig. 2c shows a representative single-point SERS spectra of 1 droplet of 10^{-6} M R6G dye printed onto the SERS substrate with self-assembled bimetallic nanostars on glass and the biosilica capsule, respectively. For both spectra, all characteristic Raman peaks were noted; however, in the presence of the biosilica capsule the signal intensity was tabulated to be 3–3.3× higher. To understand, if the observed signal variations were consequential to any inconsistencies in the nanostar deposition on the two substrates, surface density analysis was performed. We observed that irrespective of the surface, nanostar deposition followed a rather similar trend with the near equal probability of having zones of uniformly attached bimetallic nanostars with randomly placed pockets of nanostar clusters. The overall nanostar densities were estimated to be similar on both the substrates. For a representative dataset, presented in Fig. S1 in the SI, the value for the area covered by nanostars on glass was estimated to be 22.8% while for biosilica it was 21.34%. Drawing an analogy from the observed density reports and with our previous work on the biosilica photonic crystals with nanoparticles,[28] we hypothesize that this augmented signal strength is contributed by enhanced electric field contribution from the photonic crystal effect in the biosilica capsule.

Numerical simulation of bimetallic nanostars on biosilica capsules

To validate and fully understand the contribution of plasmonic nanostars and diatom photonic crystal biosilica coupling, we performed an optical simulation study. We investigated the optical field enhancement using three-dimensional finite-difference time-domain (3D-FDTD) simulations using Lumerical FDTD. The biosilica capsule was modeled based on high-resolution SEM images presented in Fig. S2 (SI). The biosilica capsule comprises a periodic porous structure made of a two-layer configuration. The upper layer consists of a 120 nm-thick silica slab with a square lattice of air holes with a periodicity of 300 nm and a hole diameter of 160 nm. The bottom layer has a thickness of 60 nm with finer structural variations. To accurately model the photonic crystal effect, we implemented a 5 × 5 unit-cell arrangement of the biosilica capsule structure in our simulations, as shown in Fig. 3b. This periodicity supports guided-mode resonance (GMR) and surface lattice resonance (SLR) and modifies the local density of optical states (LDOS) and enhances the local field intensity.[36–39] Such modifications are pivotal in enhancing the SERS signal by strengthening the light–matter interactions at the nanoscale. The incident light is a 638 nm wavelength Gaussian beam with a diameter of 1.5 μm to replicate the laser light spot of our experimental measurement.

The simulated nanostars have a tip-to-tip length of 60 ± 10 nm, matching the TEM-measured size distribution. The nanostars were modeled using a bimetallic core–spike architecture: the central core region was Ag, while each protruding spike was modeled using Au. This configuration reflects the experimentally observed elemental distribution, where Ag is concentrated near the center and Au dominates the spike regions. A representative scheme of the bimetallic nanostar structure adopted for numerical studies is shown in Fig. S3, in the SI. For computational efficiency, the 3D nanostar was simplified into a symmetric 2D flat geometry. The unique geometry of nanostars support the enhanced

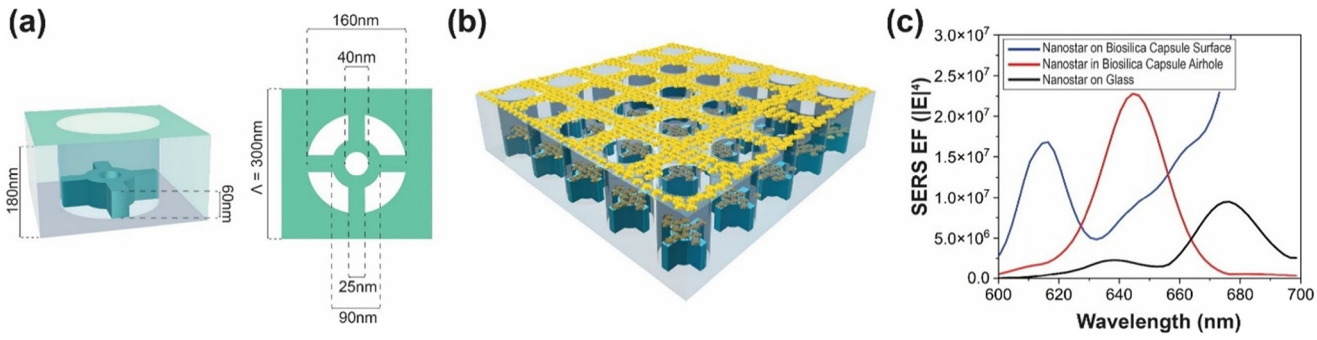

Fig. 3 (a) 3D side-view and top-view of the biosilica capsule unit cell; (b) 3D image of randomly distributed nanostars on a 5 × 5 unit cell biosilica capsule; and (c) comparison of SERS EFs of a single nanostar placed on the biosilica capsule surface (blue), airhole (red) and glass (black).

near-field electromagnetic intensity at the sharp tips known as plasmonic hot spots.[39,40] This enhanced electromagnetic field dramatically boosts signal detection sensitivity. The SERS enhancement factor (EF) is calculated as the fourth power of the electric field magnitude ($|E|^4$).[32,41] However, the experimentally observed SERS EF varies depending on multiple factors, including the analyte concentration, spatial distribution of analyte molecules, and local field fluctuations.[42] We conducted a systematic investigation of the photonic crystal influence on the nanostars' plasmonic response by placing a single bimetallic nanostar at three different locations: (i) on the capsule surface, (ii) inside an air hole of the capsule, and (iii) on a plain glass substrate. The SERS EF was calculated for each nanostar at different positions and plotted as a function of wavelength, as shown in Fig. 3c. The results indicate that at the target excitation wavelength of 638 nm, the EF for the bimetallic nanostar located on the capsule surface or inside the pore is 5 to 10 times higher than that on a plain glass substrate, consistent with previous studies on regular nanoparticles.[32,43]

To investigate this effect further, randomly distributed nanostars were simulated on both the biosilica capsule and glass. A similar 5 × 5 unit-cell structure was used for the biosilica capsule as the previous simulation, and the distribution of nanostars on the biosilica capsule and on the glass substrate was identical. We also calculated the local electric field ($|E|^4$) enhancement distribution around the nanostars for both cases at the excitation wavelength of 638 nm, as shown in Fig. 4a and b. Fig. 4a shows the electric field distribution ($|E|^4$) on the glass substrate, while Fig. 4b shows that on the biosilica capsule in the same scale, respectively. The comparison of these two cases clearly indicates a significantly higher intensity of electromagnetic hot spots in the nanostar–biosilica capsule case compared to the nanostar-on-glass substrate. Here, we define hot spots as regions where the ($|E|^4$) enhancement exceeds 10^2. We analyzed the probability distribution of electromagnetic intensities on the biosilica capsule (blue) and on glass (red) to quantify our observations, as shown in Fig. 4c. The analysis demonstrates that nanostars on the biosilica capsule consistently exhibit a higher probability of the SERS EF across the entire hotspot intensity range. To further compare the enhancement, we ranked the top 5 percent hot spot pixels based on their SERS EF, which is depicted in Fig. 4d. Notably, the SERS EF values between 10^4 and 10^6 contribute most to SERS sensing. This ranking provides a direct comparison of the electric field enhancement experienced by nanostars on both substrates. The difference between the two curves in Fig. 4d indicates that nanostars on the biosilica capsule provide stronger localized field enhancements, supporting our hypothesis that the photonic crystal structure of the diatom contributes significantly to the observed SERS EF. The results show that while both substrates exhibit an increasing trend in the enhancement as the hot spot pixel number rises, the biosilica-based substrate consistently outperforms the glass counterpart across the entire hot spot distribution. This confirms that the photonic crystal properties of the biosilica capsule play a vital role in enhancing SERS detection.

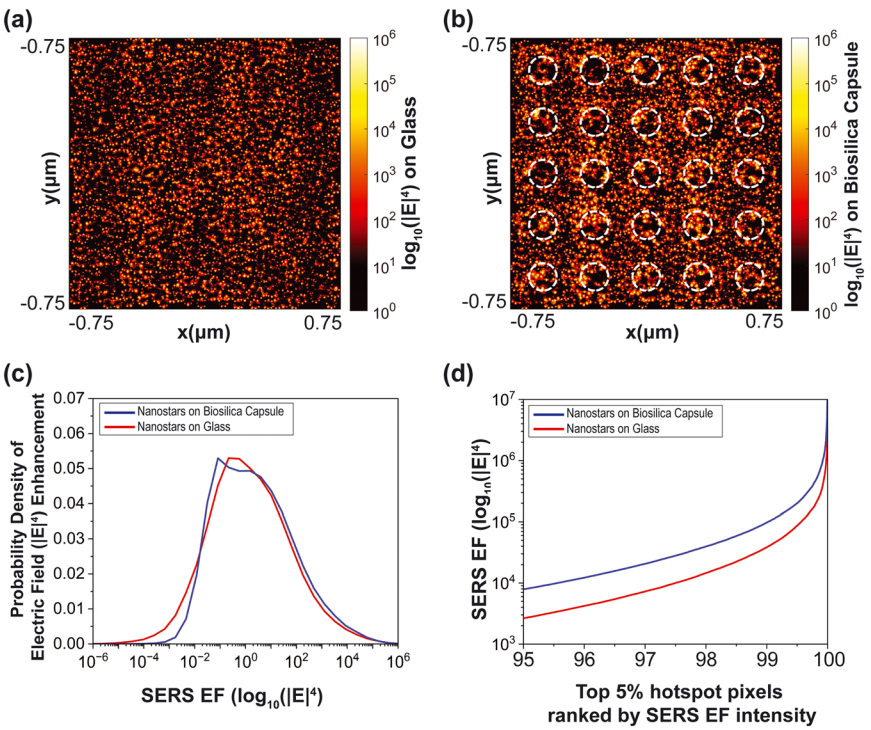

Fig. 4 Electric field enhancement ($|E|^4$) for (a) randomly distributed nanostars on glass and (b) nanostars on the biosilica capsule. (c) Probability distribution of the SERS EF around the nanostars; and (d) the SERS EF plotted as a function of the top 5% pixel number, ranked by low to high SERS EFs. In (c) and (d), the results for nanostars on the biosilica capsule are shown in blue, while those on glass are in red at a wavelength of 638 nm.

The SERS EF observed in the bimetallic nanostar–biosilica capsule case is due to several key effects. The photonic band structure of the biosilica modifies the local electromagnetic field distribution by supporting GMR and SLR, which spatially redistribute and confine the electromagnetic field, increasing its localization near the nanostars. This near-field confinement is crucial for boosting the Raman signal intensity.[44,45] Additionally, coupling between the plasmonic mode of the bimetallic nanostars and the GMR or SLR of the biosilica structure leads to the formation of a hybridized mode, which enhances the LDOS and contributes to further field enhancement.[46,47] Another contributing factor is the refractive index contrast between the biosilica and its surrounding medium, which induces strong in-plane scattering. This effect increases light–matter interactions and enhances near-field coupling with the nanostars.[48] In contrast, only localized plasmonic effects affect the field enhancement for nanostars placed directly on a plain glass substrate. These results highlight that the nanostars placed on biosilica capsules significantly enhance the local electromagnetic field, thereby improving SERS characterization.

SERS measurements of inkjet-printed R6G on bimetallic nanostar–biosilica capsules

To evaluate the sensitivity to attain SM detection, various concentrations (10^{-6} to 10^{-15} M) of R6G were inkjet-printed onto the plasmonic–biosilica capsule. The representative SERS spectrum for each tested R6G concentration is shown in Fig. 5a. For all tested concentrations, the characteristic peaks,[49] indexing well to the stretching modes in R6G were clearly visible. As expected, with the concentration decreasing from 10^{-6} to 10^{-15} M, as the number of molecules decrease, a sequential drop in the intensity is observed. The lowest concentration of R6G detected is noted to be 10^{-15} M.

At the highest R6G concentration tested at 10^{-6} M, 1 droplet equivalent to ~60 pL was enough to acquire the recorded spectrum intensity. As we move towards lower concentrations, we need a greater number of molecules or more droplets of R6G to deliver enough molecules in the detection volume for statistically significant SERS signals. However, at none of the R6G concentrations, tested under the stipulated study, more than 2000 droplets (~120 nL) of the sample volume were utilized, which is significantly lower compared to previous reports in the literature as summarized in Table 2. Mathematically, for an LOD concentration of 10^{-15} M at a 120 nL volume containing only 72 R6G molecules, dispensed over an approximately 100 μm diameter area, the probability of detecting a single molecule within the laser spot (1.03 μm) of the Raman microscope is only 1/130, which can guarantee SM optofluidic-SERS sensing if meaningful signals are detected.

We also performed some control SERS tests using a traditional soaking method for analyte deposition to emphasize the role of inkjet dispensing in achieving the said LOD. During our control tests, we noted that a) with traditional soaking, the achieved LOD was 10^{-12} M and no signal for 10^{-15} M could be recorded (SI Fig. S4 and S5) b) for the same dye concentration. Inkjet-printed substrates obtained stronger signals and required a significantly less analyte volume (SI Fig. S6). Thereby, the achieved LOD is a synergic contribution from both the presence of nanostars on the biosilica capsule and the adopted printing methodology.

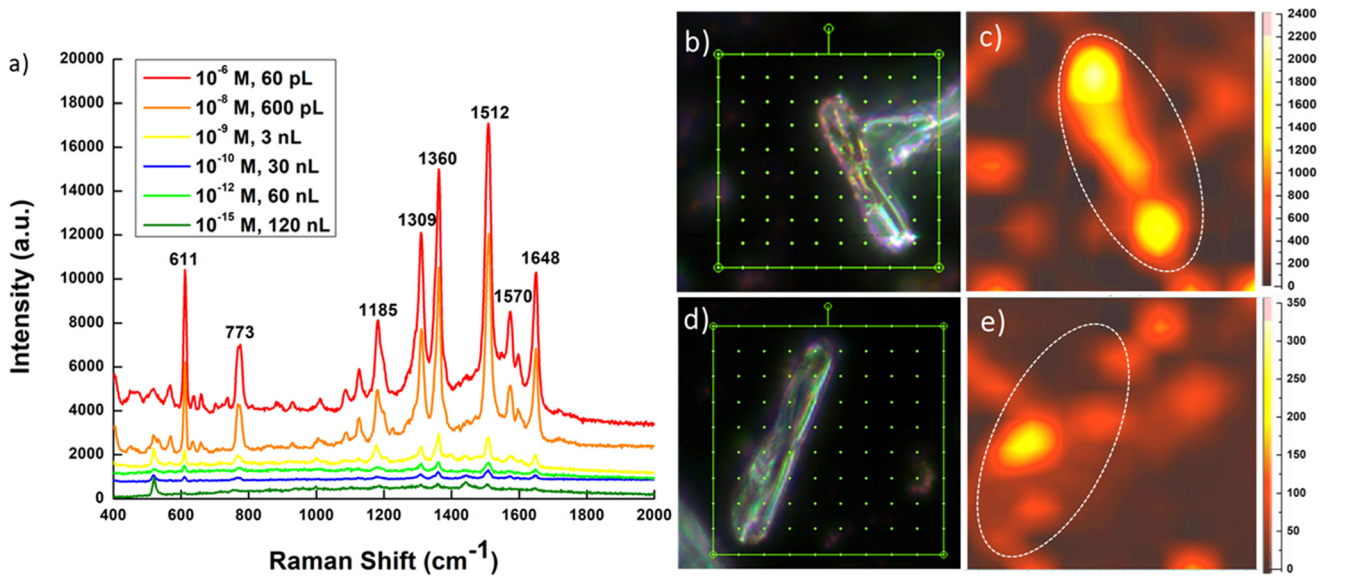

Fig. 5 a) SERS spectra of R6G at different concentrations from 10^{-6} to 10^{-15} M collected on the bimetallic nanostar–biosilica capsule; b) and d) dark-field optical images of the selected biosilica capsule used for the SERS mapping of the highest (10^{-6} M) and lowest (10^{-15} M) tested R6G concentrations; c) and e) corresponding SERS maps of the 1512 cm^{-1} Raman vibrations of R6G at 10^{-6} and 10^{-15} M, respectively. Dotted lines represent the biosilica capsule boundary.

Table 2 Comparison of optofluidic-SERS sensing using inkjet-printed dispensing techniques

S. No	SERS substrate	Printed component	Analyte	LOD of concentration	LOD of mass	Ref.
1.	Ag nanoparticle (1 nL–10 pL)	Ag nanoparticles & analyte	Alizarin	10^{-5} M	2.4×10^{-14} g	50
2.	Ag nanoparticles/chromatography paper	Nanoparticles	R6G	—	9.5×10^{-14} g	51
3.	Au nanoparticles/hydrophobic Si wafer	Nanoparticles	R6G	10^{-10} M	2.4×10^{-11} g	52
4.	Ag nanoparticles with chitosan nano-wrinkles	Nanoparticles	R6G	10^{-13} M	Unknown	53
5.	Au/Ag bimetallic nanostars on biosilica capsules (this work)	Analyte	R6G	10^{-15} M	5.7×10^{-20} g (72 molecules)	This work

While nanostars improve the sensitivity, the drop-on-demand printing system helps decrease the analyte volume required for viable measurements by effectively delivering analyte molecules to the surface of the SERS substrate. In a previous study by our research group,[32] we noted that when the small-volume droplet dispenses onto the biosilica surface, it establishes a spontaneous analyte flow. Facilitated *via* the hydrophilic nature of the diatom biosilica, this flow concentrates most of the analyte molecules within the capsule improving the local analyte concentration and thus assisting signal acquisition.

Fig. 5c and e show representative SERS maps of R6G at 10^{-6} and 10^{-15} M concentrations, respectively. A total of 100 SERS spectra (for each concentration) within the scanning range divided into 10 × 10 grids as shown in the dark-field optical image (Fig. 5b and d) were acquired. Corresponding SERS maps for the characteristic R6G vibration at 1512 cm^{-1} correlating with the biosilica capsule morphology (dotted white lines) was observed. For 10^{-6} M R6G, the signal spread fairly uniformly across the entire length and width of the biosilica capsule, indicating well distributed R6G molecules in the biosilica capsule. Contrastingly, for 10^{-15} M R6G, SERS signals were rather concentrated to a small region in the entire capsule with only a few exceptionally high signal data points replicating an "on" and "off" state, typical of single-molecule detection.

Spatially resolved SERS maps in Fig. 6 for all tested R6G concentrations were further acquired to evaluate the nature of signal generation over the SERS substrate. In these maps, each square pixel corresponds to a data point from where the signal was generated while the dotted lines represent the biosilica capsule boundary in the scanning area. The colour bars adjoining the maps indicate the signal intensity for the characteristic 1360 cm^{-1} R6G peak. Uniform at higher

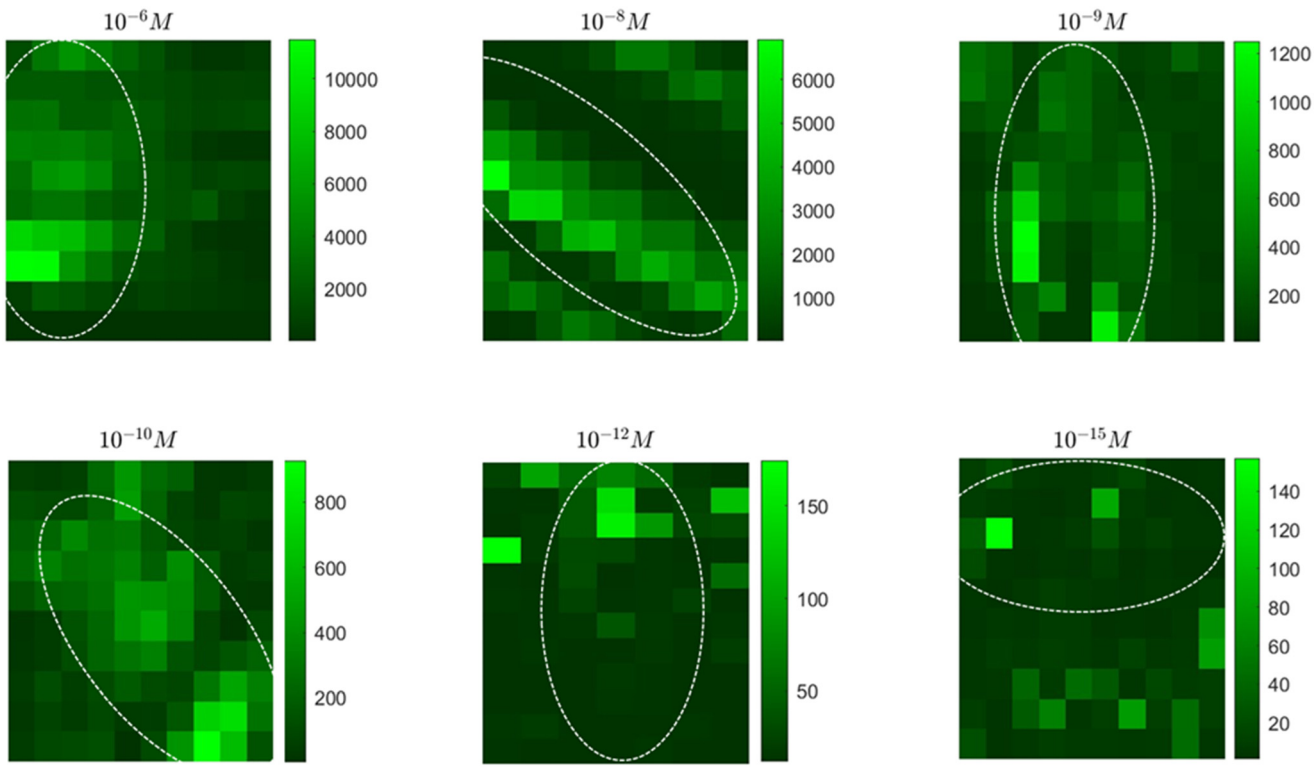

Fig. 6 10 × 10 SERS mapping of a single diatom *Pinnularia* sp. frustule printed with different concentrations of R6G dye, representing the integrated intensity of the 1360 cm^{-1} peak. Dotted lines represent the diatom frustule dimension in the tested area.

concentrations, with the decreasing analyte, both, the SERS signal intensity, and the effective data points available for signal acquisition were reduced. At none of the tested concentrations, however, the background signal appears to be higher or equivalent to the signal intensity on the biosilica capsule self-assembled with nanostars indicating that, a) most of the R6G molecules were accumulated within the diatom photonic crystal and b) the bimetallic nanostars on the biosilica capsule serve as a superior SERS material compared to nanostars alone.

Reproducibility is critical for SM SERS analysis. We printed 20 different frustules with 120 nL of 10^{-15} M R6G dye for generating the reproducibility trend and estimation of the relative standard deviation (RSD). We approximated an RSD of 40% for the tested LOD of 72 molecules (SI Fig. S7). For further detailed analysis and verification of the effect, we recorded mapped SERS signals from 10 different biosilica capsules each printed with 120 nL of the 10^{-15} M R6G solution, which contains only 72 R6G molecules. If we assume that the dispensed R6G molecules are uniformly distributed across the 100 μm diameter dispensing area and the laser spot of the confocal Raman microscope is 1.03 μm with the 50× objective lens, the probability of finding an R6G molecule within the laser spot is only 1/130. With a 10 × 10 SERS mapping, the possibility of hitting an R6G molecule is only 0.72, which represents a true single-molecule SERS detection regime. Fig. 7a shows 10 representative SERS maps with dotted elliptical circles indicating the position of diatom biosilica frustules. It clearly shows that the strongest hot spot in each map, most likely due to the presence of a single R6G molecule, is exclusively located within the frustule, although the strength varies due to different electric field EFs of plasmonic nanostars. Besides the strongest hot spot, there are also a few other hot spots within the frustule adjacent to the strongest one such as frustule 05 and 08, which could possibly be the same R6G molecule generating cross talk to the SERS mapping due to the small scanning step (~2 μm). There are also a couple of frustules (04 and 06) showing a well-separated hot spot from the strongest spot, which are mostly likely due to another R6G molecule. Our previous optofluidic SERS work proves that the hydrophilic surface of diatom frustules can enrich the molecular distribution due to evaporation-induced spontaneous flow on hydrophilic

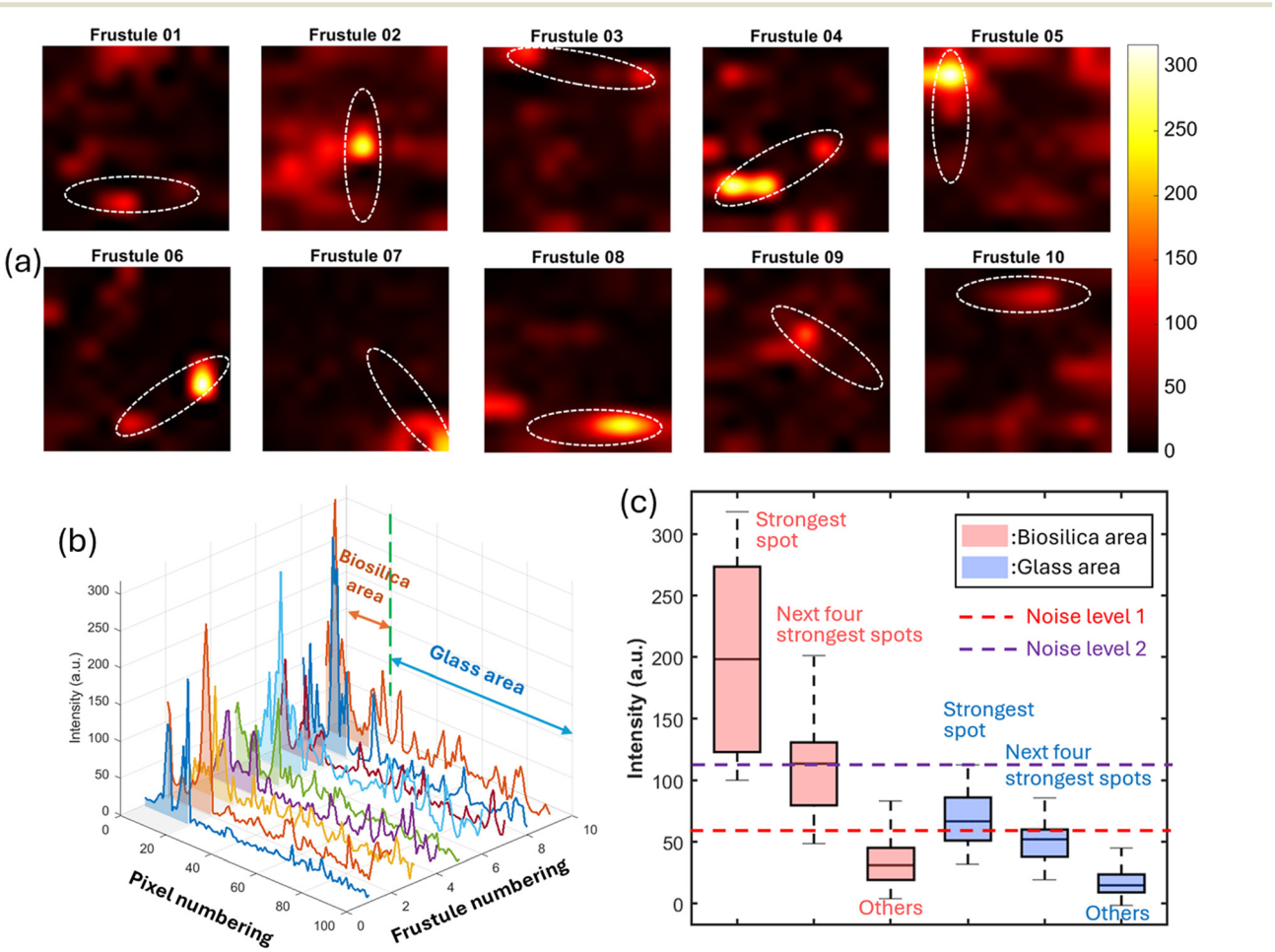

Fig. 7 a) SERS maps of 10 individual biosilica capsules printed with 120 nL 10^{-15} M R6G solution, representing the integrated intensity of the 1360 cm^{-1} peak. Dotted lines represent the diatom frustule dimension in the testing area. b) Replotted SERS intensity by expanding the pixels of SERS maps with the biosilica area first. c) Statistical analysis of classified pixels on biosilica and on the glass area for SM analysis.

biosilica capsules.[32] Therefore, it is possible to attract more than one R6G molecules within the biosilica capsule although the average SM probability is only 0.72. To compare the SERS signal strength of nanostars on the frustule and on the glass substrate, we replotted the SERS mapping results in Fig. 7b according to the pixel number. For easier visualization, we plotted those pixels on diatom biosilica first (~20 pixels in each map), followed by pixels on the glass substrate (~80 pixels). By further statistical analysis, we classified those pixels on biosilica and on glass into three categories: the "strongest spot" for high possibility SM sensing, the "next four strongest spots" for low possibility SM case, and "others" representing the background noise. The mean value and standard deviation of these classified pixels are plotted in Fig. 7c. We consider two different noise levels to determine SM detection. First, if we use 3× the mean value of the "others on glass area" as noise level 1 marked in the figure as the threshold; all 10 biosilica capsules show SM SERS detection, while only 5 strongest spots on the glass area achieve SM detection. More importantly, the biosilica capsule shows an average signal-to-noise ratio (SNR) of 3.7, while the average SNR of the strongest spot on glass is only 1.3. The biosilica capsule improved the SNR by almost 3×. Second, using a more rigorous standard of 3× the mean value of "others on biosilica" as noise level 2 in Fig. 7c, 9 out of 10 of the strongest spots in the biosilica area can be classified as the SM case, while only 1 out of the 10 strongest spots on glass can be deemed as SM sensing. In addition, about 40% of the "next four strongest spots" on biosilica are SM sensing. Overall, 90% of the possibility of SM detection and 40% of the possibility of multi-molecule sensing on diatoms qualitatively matches statistical expectation. As a comparison, the possibility of detecting a single R6G molecule on nanostar-on-glass is only 10% because of weaker SERS enhancement and accumulation of R6G molecules on the hydrophilic frustule surface. Therefore, biosilica capsules improve the SM detection possibility by 9×.

To further validate the occurrence of the SERS signals as a statistically independent rare event contributed from single-molecule signal generation with negligible contribution from other interfering factors such as photobleaching and/or clustering, a statistical analysis over ten, 10 × 10 Raman mappings (N = 1000 spots) was performed (SI Fig. S8). The intensity histogram from the stipulated dataset was observed to be long-tailed and right-skewed (skew = 6.99; kurt = 72.39) while the empirical cumulative distribution function (ECDF) experienced a sharp rise at low intensities following a flattening trend towards the tail. The results imply that only a small subset of hotspots show strong signals while the rest remain close to the basal level. Upon applying a robust threshold (median + $5\sigma_{MAD}$ and thr = 109.8 a.u.), we further obtained the event count distribution for the dataset (Fig. S8(b)). The event count per mapping data were indexed well to fit a Poisson trend ($\hat{\lambda}$ = 6.6; χ^2 = 4.12; df = 3; p = 0.25) iterating the occurrence of signal generation in the SM regime.

Conclusions

In this work, we report a reproducible, SM optofluidic-SERS substrate developed by chemically anchoring Au/Ag bimetallic nanostars to *Pinnularia* sp. biosilica capsules. In comparison to the SERS substrate using only bimetallic nanostars, we observed approximately 3× improvement in SERS signals due to the biosilica capsule. The SERS enhancement was validated through numerical studies, where nanostars attached to the photonic crystal biosilica were characterized with universally improved EFs, indicating better hot-spot engineering. In addition to enhanced sensitivity, our twin aim of the study to achieve reproducibility was attained using a drop-on-demand inkjet printing device for precise analysis and efficient analyte delivery. Using R6G as the testing analyte, we attained an effective mass LOD of 5.7×10^{-20} gram, or 72 R6G molecules from 120 nL of 10^{-15} M solution. Through the 10 SERS mapping data of individual biosilica capsules, we confirmed the SM SERS signals within the scanned area. Statistical analysis of the mapping data over the cell-sized biosilica capsule achieved a 3× higher SNR ratio and 9× better SM detection possibility compared to that on the glass substrate. In summary, the cell-sized biosilica capsule based on the diatom *Pinnularia* sp. frustule decorated with high-density bimetallic nanostars can be an effective substrate for reproducible single-molecule optofluidic-SERS analysis.

Author contributions

Subhavna Juneja: conceptualization and methodology (experimental studies), investigation, validation, formal analysis, visualisation, and writing – original draft and reviewing and editing. Sudipta Biswas: methodology (numerical studies), investigation, formal analysis, visualization, and writing – original draft and reviewing. Kang Rong: investigation, formal analysis, visualization, and writing – reviewing. Alan X. Wang: conceptualisation, methodology, validation, supervision, writing – reviewing and editing, funding acquisition, and project administration. All the contributing authors have been included and approve to the final version of the manuscript submitted.

Conflicts of interest

The authors declare no competing financial interest.

Data availability

Diatom cultivation, diatom photonic crystal isolation, synthesis of bimetallic nanostars, self-assembly of bimetallic nanostars on diatom photonic crystals, and characterization details are available in the supplementary information (SI).

Supplementary information is available. See DOI: https://doi.org/10.1039/d5sd00161g.

Acknowledgements

This work was financially supported by the Baylor University Mearse Chair Endowment Fund in Biological and Biomedical Engineering. The authors would like to thank Prof. Zhenrong Zhang and her team for helping with the UV-visible equipment for the measurements.

References

1 J. Kneipp, H. Kneipp and K. Kneipp, SERS—a Single-Molecule and Nanoscale Tool for Bioanalytics, *Chem. Soc. Rev.*, 2008, **37**, 1052–1060.
2 C. H. Lee, L. Tian and S. Singamaneni, Paper-Based SERS Swab for Rapid Trace Detection on Real-World Surfaces, *ACS Appl. Mater. Interfaces*, 2010, **2**(12), 3429–3435.
3 R. A. Alvarez-Puebla and L. M. Liz-Marzán, SERS Detection of Small Inorganic Molecules and Ions, *Angew. Chem., Int. Ed.*, 2012, **51**, 11214–11223.
4 K. Kneipp, Y. Wang, H. Harald Kneipp, L. T. Perelman, I. Itzkan, R. R. Dasari and M. S. Feld, Single Molecule Detection Using Surface-Enhanced Raman Scattering (SERS), *Phys. Rev. Lett.*, 1997, **78**(9), 1667–1670.
5 D. Radziuk and H. Moehwald, Prospects for Plasmonic Hot Spots in Single Molecule SERS Towards the Chemical Imaging of Live Cells, *Phys. Chem. Chem. Phys.*, 2015, **17**, 21072–21093.
6 J. Jiang, K. Bosnick, M. Maillard and L. Brus, Single Molecule Raman Spectroscopy at the Junctions of Large Ag Nanocrystals, *J. Phys. Chem. B*, 2003, **107**(37), 9964–9972.
7 L. Zhang, H. Liu, L. Chen, P. Guan, B. Chen, T. Fujita, Y. Yamaguchi, H. Iwasaki, Q.-K. Xue and M. Chen, Large-scale Growth of Sharp Gold Nano-Cones for Single-Molecule SERS Detection, *RSC Adv.*, 2016, **6**, 2882–2887.
8 P. Alonso-González, P. Albella, M. Schnell, J. Chen, F. Huth, A. García-Etxarri, F. Casanova, F. Golmar, L. Arzubiaga, L. E. Hueso, J. Aizpurua and R. Hillenbrand, Resolving the Electromagnetic Mechanism of Surface-Enhanced Light Scattering at Single Hot Spots, *Nat. Commun.*, 2012, **3**, 684.
9 L. Fabris, M. Dante, T. Nguyen, J. B.-H. Tok and G. C. Bazan, SERS Aptatags: New Responsive Metallic Nanostructures for Heterogeneous Protein Detection by Surface Enhanced Raman Spectroscopy, *Adv. Funct. Mater.*, 2008, **18**, 2518–2525.
10 J. Reguera, J. Langer, D. Jiménez de Aberasturi and L. M. Liz-Marzán, Anisotropic Metal Nanoparticles for Surface Enhanced Raman Scattering, *Chem. Soc. Rev.*, 2017, **46**, 3866–3885.
11 X. Xu, H. Li, D. Hasan, R. S. Ruoff, A. X. Wang and D. L. Fan, Near-Field Enhanced Plasmonic-Magnetic Bifunctional Nanotubes for Single Cell Bioanalysis, *Adv. Funct. Mater.*, 2013, **23**(35), 4332–4338.
12 P. Anantha, P. Raj, P. Zheng, S. Tanwar and I. Barman, Gold Nanoprism Enhanced SERS Aptasensor for Simultaneous Detection of Thrombin and VEGF, *Sens. Actuators, B*, 2025, **423**, 136811.
13 N. T. Tran, T.-G. Nguyen, M.-T. Le, K.-S. Trinh, V.-D. Phung, A.-T. N. Huynh and N.-T. Pham, Highly Branched and Hollow Gold Nanourchins for Bacterial Killing and Off-Resonance SERS Sensing, *Chem. Pap.*, 2023, **77**, 7505–7514.
14 X. Meng, J. Dyer, Y. Huo and C. Jiang, Greater SERS Activity of Ligand-Stabilized Gold Nanostars with Sharp Branches, *Langmuir*, 2020, **36**(13), 3558–3564.
15 Y. Wang, L. Polavarapu and L. M. Liz-Marzán, Reduced Graphene Oxide-Supported Gold Nanostars for Improved SERS Sensing and Drug Delivery, *ACS Appl. Mater. Interfaces*, 2014, **6**(24), 21798–21805.
16 A. Li, L. Tang, D. Song, S. Song, W. Ma, L. Xu, H. Kuang, X. Wu, L. Liu, X. Chen and C. Xu, A SERS-Active Sensor Based on Heterogeneous Gold Nanostar Core–Silver Nanoparticle Satellite Assemblies for Ultrasensitive Detection of AflatoxinB1, *Nanoscale*, 2016, **8**, 1873–1878.
17 X. Qi, X. Wang, Y. Dong, J. Xie, X. Gui, J. Bai, J. Duan, J. Liu and H. Yao, Fast Synthesis of Gold Nanostar SERS Substrates Based on Ion-Track Etched Membrane by One-Step Redox Reaction, *Spectrochim. Acta, Part A*, 2002, **272**, 120955.
18 A. S. D. S. Indrasekara, S. Meyers, S. Shubeita, L. C. Feldman, T. Gustafsson and L. Fabris, Gold Nanostar Substrates for SERS-Based Chemical Sensing in the Femtomolar Regime, *Nanoscale*, 2014, **6**, 8891–8899.
19 S. Harmsen, R. Huang, M. A. Wall, H. Karabeber, J. M. Samii, M. Spaliviero, J. R. White, S. Monette, R. O'Connor, K. L. Pitter, S. A. Sastra, M. Saborowski, E. C. Holland, S. Singer, K. P. Olive, S. W. Lowe, R. G. Blasberg and M. F. Kircher, Surface-enhanced Resonance Raman Scattering Nanostars for High-Precision Cancer Imaging, *Sci. Transl. Med.*, 2015, **7**(271), 271ra7.
20 S. L. Kitaw, Y. W. Ahmed, A. Candra, T.-Y. Wu, B. E. Anley, Y.-Y. Chen, Y.-T. Cheng, K.-J. Chen, C. Thammaniphit, C. C. Hsu, Y. T. Wu, M. H. Khana and H.-C. Tsai, An Advanced Plasmonic Bimetallic Nanostar Composite for Ultra-Sensitive SERS Detection of Crystal Violet, *Nanoscale*, 2025, **17**, 508–519.
21 Y.-L. Li, J. Zhu, G.-J. Weng, Y.-N. Liu, J.-J. Li and W.-J. Zhao, Study on the Roughen Process of Branches of AuAg Nanostars for the Improved Surface-Enhanced Raman Scattering (SERS) to Detect Crystal Violet in Fish, *Sens. Actuators, B*, 2023, **390**, 133936.
22 R. A. Harder, L. A. Wijenayaka, H. T. Phan and A. J. Haes, Tuning Gold Nanostar Morphology for the SERS Detection of Uranyl, *J. Raman Spectrosc.*, 2021, **52**(2), 497–505.
23 A. Garg, E. Mejia, W. Nam, M. Nie, W. Wang, P. Vikesland and W. Zhou, Microporous Multiresonant Plasmonic Meshes by Hierarchical Micro–Nanoimprinting for Bio-Interfaced SERS Imaging and Nonlinear Nano-Optics, *Small*, 2022, **18**(15), 2106887.
24 M. Li, F. Zhao, J. Zeng, J. Qi, J. Lu and W. C. Shih, Microfluidic Surface-Enhanced Raman Scattering Sensor with Monolithically Integrated Nanoporous Gold Disk Arrays for Rapid and Label-Free Biomolecular Detection, *J. Biomed. Opt.*, 2014, **19**(11), 111611.

25 E. De Tommasi and A. C. De Luca, Diatom biosilica in plasmonics: applications in sensing, diagnostics and therapeutics, *Biomed. Opt. Express*, 2022, **13**(5), 3080–3101.
26 K. Sivashanmugan, K. Squire, J. A. Kraai, A. Tan, Y. Zhao, G. L. Rorrer and A. X. Wang, Biological Photonic Crystal-Enhanced Plasmonic Mesocapsules: Approaching Single-Molecule Optofluidic-SERS Sensing, *Adv. Opt. Mater.*, 2019, **7**, 1900415.
27 J. A. Kraai, X. Alan, A. X. Wang and G. L. Rorrer, Photonic Crystal Enhanced SERS Detection of Analytes Separated by Ultrathin Layer Chromatography Using a Diatom Frustule Monolayer, *Adv. Mater. Interfaces*, 2020, **7**(11), 2000191.
28 F. Ren, J. Campbell, G. L. Rorrer and A. X. Wang, Surface-Enhanced Raman Spectroscopy Sensors from Nanobiosilica with Self-Assembled Plasmonic Nanoparticles, *IEEE J. Quantum Electron.*, 2014, **20**(3), 6900806.
29 K. J. Squire, Y. Zhao, A. Tan, K. Sivashanmugan, J. A. Kraai, L. Gregory, G. L. Rorrer and A. X. Wang, Photonic Crystal-Enhanced Fluorescence Imaging Immunoassay for Cardiovascular Disease Biomarker Screening with Machine Learning Analysis, *Sens. Actuators, B*, 2019, **290**, 118–124.
30 S. Juneja, B. Zhang and A. X. Wang, Limit-Defying μ-Total Analysis System: Achieving Part-Per-Quadrillion Sensitivity on a Hierarchical Optofluidic SERS Sensor, *ACS Omega*, 2023, **8**(19), 17151–17158.
31 S. Atta and T. Vo-Din, Bimetallic Gold Nanostars Having High Aspect Ratio Spikes for Sensitive Surface-Enhanced Raman Scattering Sensing, *ACS Appl. Nano Mater.*, 2022, **5**(9), 12562–12570.
32 X. Kong, Y. Xi, P. LeDuff, E. Li, Y. Liu, L.-J. Cheng, G. L. Rorrer, H. Tan and A. X. Wang, Optofluidic Sensing from Inkjet-Printed Droplets: The Enormous Enhancement by Evaporation-Induced Spontaneous Flow on Photonic Crystal Biosilica, *Nanoscale*, 2016, **8**, 17285.
33 S. Atta, A. J. Canning and T. Vo-Dinh, A Simple Low-Cost Flexible Plasmonic Patch Based on Spiky Gold Nanostars for Ultra-Sensitive SERS Sensing, *Analyst*, 2024, **149**, 2084–2096.
34 S. Atta, M. Beetz and L. Fabris, Understanding the Role of AgNO3 Concentration and Seed Morphology in the Achievement of Tunable Shape Control in Gold Nanostars, *Nanoscale*, 2019, **11**, 2946–2958.
35 H. R. Nikabadi, N. Shahtahmasebi, M. R. Rokn-Abadi, M. Karimipour and M. M. B. Mohagheghi, Structural Verification and Optical Characterization of SiO_2–Au–Cu_2O Nanoparticles, *Bull. Mater. Sci.*, 2014, **37**(3), 527–532.
36 P. Lalanne, W. Yan, K. Vynck, C. Sauvan and J.-P. Hugonin, Light Interaction with Photonic and Plasmonic Resonances, *Laser Photonics Rev.*, 2018, **12**(5), 1700113.
37 B. Auguié and W. L. Barnes, Collective Resonances in Gold Nanoparticle Arrays, *Phys. Rev. Lett.*, 2008, **101**(14), 143902.
38 G. W. Castellanos, P. Bai and J. G. Rivas, Lattice Resonances in Dielectric Metasurfaces, *J. Appl. Phys.*, 2019, **125**(21), 213105.
39 P. Etchegoin and E. C. L. Ru, *Principles of Surface-Enhanced Raman Spectroscopy*, Elsevier BV, 2009.
40 A. L. Koh, K. Bao, I. Khan, W. Ewen Smith, G. Kothleitner, P. Nordlander, S. A. Maier and D. W. McComb, Electron Energy-Loss Spectroscopy (EELS) of Surface Plasmons in Single Silver Nanoparticles and Dimers: Influence of Beam Damage and Mapping of Dark Modes, *ACS Nano*, 2009, **3**(10), 3015–3022.
41 C. M. Aikens, L. R. Madison and G. C. Schatz, The Effect of Field Gradient on SERS, *Nat. Photonics*, 2013, **7**(7), 508–510.
42 X. Kong, E. Li, K. Squire, Y. Liu, B. Wu, L. Cheng and A. X. Wang, Plasmonic Nanoparticles-Decorated Diatomite Biosilica: Extending the Horizon of On-Chip Chromatography and Label-Free Biosensing, *J. Biophotonics*, 2017, **10**(11), 1473–1484.
43 X. Kong, K. Squire, E. Li, P. LeDuff, G. L. Rorrer, S. Tang, B. Chen, C. P. McKay, R. Navarro-Gonzalez and A. X. Wang, Chemical and Biological Sensing Using Diatom Photonic Crystal Biosilica With In-Situ Growth Plasmonic Nanoparticles, *IEEE Trans. NanoBiosci.*, 2016, **15**(8), 828–834.
44 V. Myroshnychenko, J. Rodríguez-Fernández, I. Pastoriza-Santos, A. M. Funston, C. Novo, P. Mulvaney, L. M. Liz-Marzán and F. J. García de Abajo, Modelling the Optical Response of Gold Nanoparticles, *Chem. Soc. Rev.*, 2008, **37**(9), 1792.
45 D. E. Chang, A. S. Sørensen, P. R. Hemmer and M. D. Lukin, Strong Coupling of Single Emitters to Surface Plasmons, *Phys. Rev. B: Condens. Matter Mater. Phys.*, 2007, **76**(3), 035420.
46 S. Wu, Y. Shen and C. Jin, Surface-enhanced Raman Scattering Induced by The Coupling of the Guided Mode with Localized Surface Plasmon Resonances, *Nanoscale*, 2019, **11**(30), 14164–14173.
47 S. Lal, S. Link and N. J. Halas, Nano-optics From Sensing to Waveguiding, *Nat. Photonics*, 2007, **1**(11), 641–648.
48 W. L. Barnes, A. Dereux and T. W. Ebbesen, Surface Plasmon Subwavelength Optics, *Nature*, 2003, **424**(6950), 824–830.
49 D. Huang, J. Cui and X. Chen, A morpholinium surfactant crystallization induced formation of Au nanoparticle sheet-like assemblies with uniform SERS activity, *Colloids Surf., A*, 2014, **456**, 100–107.
50 C. Miccichè, G. Arrabito, F. Amato, G. Buscarino, S. Agnello and B. Pignataro, Inkjet printing Ag nanoparticles for SERS hot spots, *Anal. Methods*, 2018, **10**, 3215–3223.
51 W. W. Yu and I. M. White, Inkjet-printed paper-based SERS dipsticks and swabs for trace chemical detection, *Analyst*, 2013, **138**, 1020–1025.
52 Q. Yang, M. Deng, H. Li, M. Li, C. Zhang, W. Shen, Y. Li, D. Guo and Y. Song, Highly reproducible SERS arrays directly written by inkjet printing, *Nanoscale*, 2015, **7**, 421–425.
53 T. T. Thuy, M. Sharipov, Y. Lee, B. The Huy and Y.-I. Lee, Inkjet-based microreactor for the synthesis of silver nanoparticles on plasmonic paper decorated with chitosan nano-wrinkles for efficient on-site Surface-enhanced Raman Scattering (SERS), *NanoSelect*, 2020, **1**(5), 499–509.